

# Two-photon polymerization system based on a resonant scanner for high-throughput production of tissue engineering microcaffolds

Stefan Binder<sup>a,b,\*</sup>, Franziska Chalupa-Gantner<sup>a,b,1</sup>, Han Woong Yoo<sup>c</sup>,  
Tommaso Zandrini<sup>a,b</sup>, Aleksandr Ovsianikov<sup>a,b,\*</sup>

<sup>a</sup> Research Group 3D Printing and Biofabrication, Institute of Materials Science and Technology, TU Wien, Vienna 1060, Austria

<sup>b</sup> Austrian Cluster for Tissue Regeneration (<https://www.tissue-regeneration.at>), Austria

<sup>c</sup> Research Unit of Advanced Mechatronic Systems, Institute of Automation and Control, TU Wien, Vienna 1040, Austria

## ARTICLE INFO

### Keywords:

3D printing  
Two-photon polymerization  
Resonant scanner  
Microcaffolds  
Additive manufacturing  
Tissue engineering  
Photopolymerization

## ABSTRACT

Two-photon polymerization (2PP) is a 3D printing technique renowned for its outstanding resolution and the capability to produce complex structures directly within a material volume. While the technology has matured substantially since its first demonstration, the long processing times attributed to the high resolution, remain a significant obstacle for the use of 2PP in production. This study introduces a novel 2PP setup designed to address this limitation by significantly boosting the throughput, by at least one order of magnitude compared to existing commercial products. This improvement is realized through the implementation of a resonant scanner technology to rapidly direct the laser during fabrication. All optical components were selected carefully, to avoid any limitations that may emerge when the scanner is no longer the lone bottleneck for production throughput. Additionally, newly developed characterization and calibration methods, employed to optimize structuring accuracy and throughput, are discussed.

## 1. Introduction

Two-photon polymerization (2PP) is a powerful and versatile 3D printing technique that provides outstanding precision and feature resolution. Since its initial demonstration over a quarter of a century ago, 2PP has shown steady improvement[1]. The resolution has been enhanced significantly, well beyond the diffraction limit[2] and the throughput has increased by multiple orders of magnitude[3]. As a result of this progress, 2PP is approaching industrial relevance[2] and the technology's applicability has broadened to various fields, including micro-optics[4], photonics[2,5–7], microfluidics[8–11], and 3D cell culture tissue engineering scaffolds[12–16]. Furthermore, it has become feasible to fabricate upscaled high-resolution structures and enable batch production by 2PP[11,17–19].

The process of 2PP is based on 2-photon absorption (2PA). A pulsed laser is focused into a photoreactive resin, thereby initiating polymerization. Due to the non-linear nature of 2PA the polymerization is confined to a distinct volume (voxel) around the focal spot[20]. By

moving the focal point with precise temporal and spatial control within the material volume, complex high-resolution structures can be produced from a versatile range of materials[2,19,21]. Despite its versatility and recent advances, one challenge that still has to be addressed for 2PP to reach its full potential is its low throughput, which is primarily attributed to its high resolution. In order to leverage the benefits of the high resolution and achieve competitive throughput comparable to other 3D printing techniques, such as  $\mu$ SLA[22], (r2r)CLIP[23] or volumetric printing[24–26], scaling up production and enhancing fabrication speed are crucial.

The initial method of moving the laser focus through the sample material was based on linear translation stages. A significant improvement in throughput was achieved with the transition to the use of galvanometer mirror scanners that deflect the laser in the sample plane[27]. Nevertheless, despite galvo scanners being the current state-of-the-art and even being used in some commercial 2PP systems[28], the throughput is still a limitation for the translation of applications to an industrial scale.

\* Correspondence to: Research Group 3D Printing and Biofabrication, Institute of Materials Science and Technology, TU Wien, Getreidemarkt 9, 1060 Vienna, Austria.

E-mail addresses: [stefan.binder@tuwien.ac.at](mailto:stefan.binder@tuwien.ac.at) (S. Binder), [aleksandr.ovsianikov@tuwien.ac.at](mailto:aleksandr.ovsianikov@tuwien.ac.at) (A. Ovsianikov).

<sup>1</sup> Stefan Binder and Franziska Chalupa-Gantner contributed equally as first authors.

<https://doi.org/10.1016/j.addma.2024.104601>

Received 16 September 2024; Received in revised form 12 November 2024; Accepted 8 December 2024

Available online 9 December 2024

2214-8604/© 2024 The Authors. Published by Elsevier B.V. This is an open access article under the CC BY license (<http://creativecommons.org/licenses/by/4.0/>).

Consequently, ongoing research efforts focus on the development of 2PP systems that facilitate even higher production speeds [3,29]. Two possible approaches to address this limitation are sequential and parallel printing. In sequential printing, only a single voxel is polymerized at any given point in time [30]. For parallel printing in 2PP, the typical implementation involves multibeam systems where the laser is split into multiple beams, which are then scanned across different sections of the field of view (FOV) [2]. This approach comes with the drawback that the laser power is usually modulated before the beams are split, limiting the system to creating periodic structures that repeat at the same distance as the focus points' spacing [29,31,32]. Alternatively, the beam is shaped using spatial light modulation, enabling the creation of more complex shapes by dynamically adjusting the light distribution [33–35]. Nevertheless, even such systems only reach their full throughput potential with periodic structures, as otherwise not all foci can be used for simultaneously.

In contrast, sequential printing offers the ability to create designs with fewer limitations, however, at the expense of fabrication time. Nevertheless, Pearre, B.W. et al. [36] demonstrated recently that the throughput of sequential printing can be significantly improved, while avoiding the limitations of parallel printing, by using a resonant scanner. They converted a resonant scanning two-photon microscope into a 2PP printer to showcase the feasibility of a relatively cost-effective yet high-performance multipurpose device. However, not all aspects of the setup, such as the laser modulation bandwidth and the FOV, were optimized for high-throughput 2PP, potentially resulting in increased production time and lower resolution.

Here, we present the next step in high-throughput 2PP through the development of a custom-built setup utilizing a resonant scanner. Designing a system from the ground up allowed us to optimize the printing process for increased throughput without compromising the high resolution. To this end, the hardware was carefully selected and calibration and test methods were established to optimize and verify the systems' performance. We further demonstrate the potential of the resonant scanner-based system through the high-throughput fabrication of microscaffolds for tissue engineering [21], underscoring the capabilities of this approach.

## 2. Methods

### 2.1. Materials

The photoinitiator used for all 2PP processing was Michler's ethyl ketone (4,4'-Bis-(diethylamino)-benzophenone, Sigma-Aldrich). Microscaffold production was tested with a photosensitive PCL-based resin (DEGRAD INX, BIO INX) and 4 wt% photoinitiator. For other calibration test prints a 50:50 mixture of ethoxylated-(20/3)-trimethylolpropane triacrylate (ETA, Sartomer 415) and trimethylolpropane triacrylate (TTA, Genomer 1330) with 5 mM photoinitiator was used since the liquid resin more straightforward to prepare and has a much longer shelf life after preparation. To develop the samples after printing, the unpolymerized resin was washed out with Tetrahydrofuran (THF, Sigma-Aldrich, USA) in the case of DEGRAD INX or 1-Propanol (Carl Roth GmbH+ Co. KG, Germany) when using ETA:TTA.

### 2.2. 2PP setup

The 2PP setup developed in this work is based on the 515 nm output of a Yb-based femtosecond Oscillator (FLINT, Light Conversion) with a minimum pulse duration of 120 fs, a repetition rate of 76 MHz, and a maximum power of 1.9 W. The laser power is modulated by an acousto-optic modulator (AOM) (M1406-AQ175-0.5, ISOMET), which is able to achieve a modulation bandwidth of 30 MHz. Dispersion compensation of  $-18000 \text{ fs}^2$  is achieved with multiple bounces between a pair of chirped mirrors (Ultrafast Innovations). The beam is then expanded to a size of 5 mm with a pair of lenses (LA1461-A-ML and LC1120-A-ML,

Thorlabs) to match the scanner's useful aperture. The scanner consists of an 8 kHz resonant scanner (CRS 8 KHz, Cambridge Technology) with a maximum optical scan angle of  $26^\circ$  (peak-to-peak) and a galvo scanner (6215 H, Cambridge Technology) with a maximum optical scan angle of  $40^\circ$  (peak-to-peak). After the scanner, the laser passes through a scan lens (S4LFT4010/292, Sill Optics) and a custom-designed tube lens arranged in a 4 f system. The beam is then directed into a 10x NA 0.4 microscope objective (UPLXAPO10X, Olympus), which is mounted on a linear Z-stage (Z-Achse PLUS 50 mm, Märzhäuser) with a travel range of 50 mm. The objective focuses the beam with up to 630 mW into the sample, which can be translated in XY-direction by a linear stage. To enable observation of the printing process, a 1.6 megapixel CMOS camera (CS165MU/M, Thorlabs) is mounted underneath the objective behind a longpass dichroic mirror (DMLP567, Thorlabs). Schematics of the optical setup can be seen in Fig. 1 and photos of the actual setup can be found in the [supplementary material](#). The AOM amplitude and the galvo scanner position are controlled by voltage signals, which are generated by a 14-bit arbitrary waveform generator (AWG) (M2i6034-exp with M2i6-exp-4Amp, SPECTRUM Instrumentation) with an output rate of 125 MSamples/s. All hardware devices, the 2PP process, and calibration measurement routines were controlled by custom code written in Python (Version 3.10).

#### 2.2.1. Line tests

The minimum feature size parallel and perpendicular to the resonant scan direction was tested by printing single lines in both directions. The  $20 \mu\text{m}$  long lines were fabricated between  $100 \times 100 \times 100 \mu\text{m}^3$  cube structures at the same time as the corresponding cube layers. The lines parallel to the resonant scan direction were created by keeping the laser on for the duration it takes the scanner to move the length of the line. The perpendicular lines were created by printing single voxels in consecutive scan lines. After postprocessing, the lines were imaged with a scanning electron microscope (SEM) (Evo 10, Zeiss).

#### 2.2.2. AOM bandwidth and trigger accuracy measurement

A photodiode (DET100A2, Thorlabs) was mounted above the printer's objective. Positioning the photodiode 2–3 mm above the focal plane ensures the full beam is captured without damaging the sensor. Measurements are then taken by turning the AOM on twice for a certain time with the same time span between the pulses. The time steps are limited to a multiple of the duration of one sample at the maximum sample rate (62.5 MSamples/s/channel) of the AWG. The AWG's control signal and the photodiode's signal are recorded with an oscilloscope (DS1104, Rigol). The same setup was used to determine the AWG's trigger accuracy by repeating the measurement multiple times with the same output signal and measuring the variance in the duration between rise of the resonant scanner's synchronization signal and the first rise of the photodiode's signal.

#### 2.3. Field of view (FOV) power characterization

The measurement of relative laser power in the printing plane at different scan positions uses the same hardware setup as the AOM bandwidth measurement. While the laser and the resonant scanner are permanently on, the oscilloscope is triggered by the resonant scanner's sync signal, and the laser power is recorded for a duration of  $120 \mu\text{s}$ , with the trigger point being offset by  $-31 \mu\text{s}$ , so that the power over one scan line is fully within the recorded time span. This measurement is then repeated for galvo scan position from  $-1300 \mu\text{m}$  to  $1300 \mu\text{m}$  in  $20 \mu\text{m}$  steps. When plotting the resulting data as a 2D heatmap, the data points along the resonant scan direction are arranged with the same transformation that is used for positioning calculations during printing.

#### 2.4. Resonant movement synchronization

The resonant scanner's driver (Model 711–80159, Cambridge

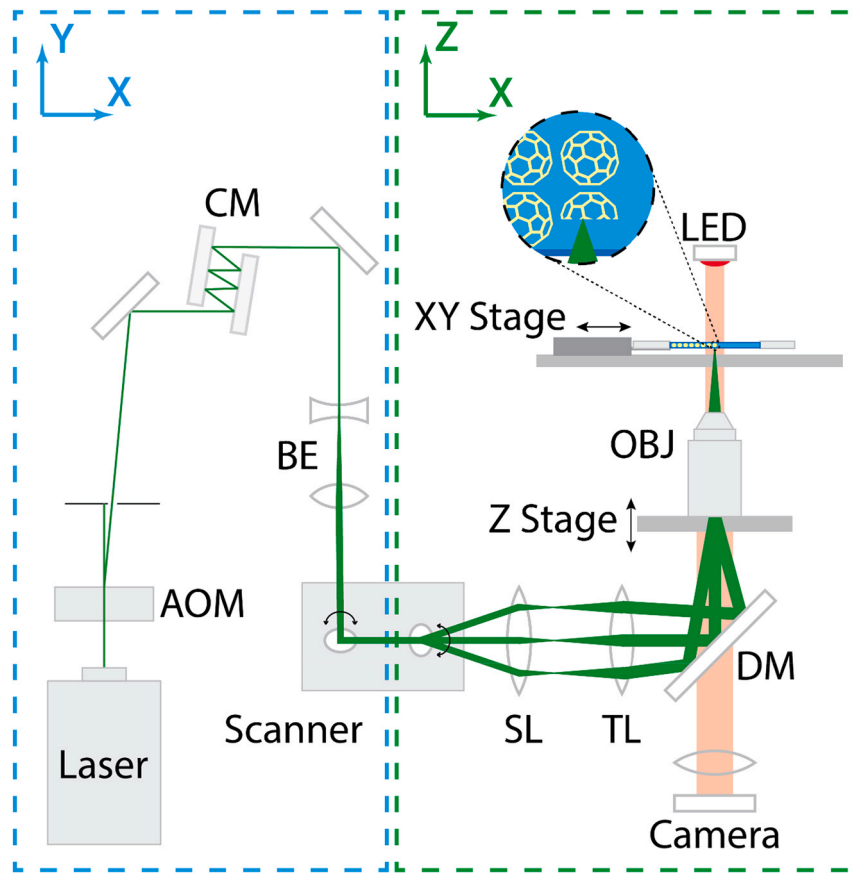


**Fig. 1. Illustration of the developed 2PP setup.** AOM: acousto-optic modulator; CM: chirped mirrors; BE: beam expander consisting of two lenses; SL: scan lens; TL: tube lens; DM: dichroic mirror; OBJ: 10x NA 0.4 microscope objective.

Technology) offers a sync signal, which is used to synchronize the resonant scanner with the other components. Ideally, the signal switches level at each change of direction of the scanner. Deviations from a 50 % duty cycle and a phase offset of the signal relative to the turnaround points can be adjusted via potentiometers on the driver. For precise control, software correction was chosen, where the output was shifted by a fixed time delay. The delay was determined by printing  $100 \times 100 \mu\text{m}$  single layer squares consisting of parallel lines with different delay settings and determining via the setup camera for which settings the overlap between the two scan directions is the most accurate.

### 2.5. Scaling and rotation

To find the scaling and rotation factors, the positioning of the XY-stage was used as a reference. Four Cube structures with a size of  $400 \times 400 \times 100 \mu\text{m}^3$  were printed consecutively, with their centers positioned on an orthogonal grid spaced out by  $400 \mu\text{m}$ . Therefore, if the scaling and rotation factors are set correctly, the sides of neighboring structures would align perfectly. By evaluating the alignment with the 2PP system's camera immediately after printing, adequately precise scaling and rotation factors can be found with only a few iterations of this process.

### 2.6. Galvo scanner jump delays

Determination of correct values for the galvo scanner's jump delay is achieved by measuring the laser beam's position with a position sensitive detector (PSD) (S2044, Hamamatsu) and recording the output with a data acquisition card (NI 9215 with cDAQ-9171, National Instruments) while performing movements with the galvo scanner. The PSD was mounted above the printer's objective with the sensor's surface

positioned a few hundred micrometers above the objective focal plane to achieve a laser spot size close to the optimum for the sensor of  $200 \mu\text{m}$ . This distance from the focal plane leads to the PSD delivering values that don't fully reflect the exact movement of the laser's focal spot unless the objective's back focal plane is fully illuminated at all scan angles, which is potentially not the case, depending on the objective's z-position. The distortions due to this effect and non-linearities in the sensor's measurement behavior make calibration necessary. As measuring the dynamic positioning behavior was of main interest, static positioning was used as a reference for the measurement. For the calibration, the galvo scanner was set to a range of positions for 2 ms, which is enough time for the scanner to settle in position and record the PSD signal for each position. The acquired values were then fitted with a polynomial, which was used for converting PSD signal to a position in subsequent experiments. It is important to note that the positions obtained by this conversion can be compared to the scanner's control signal but don't necessarily represent the physical laser spot position due to the fact that a non-linear relation between scanner position and control signal would not be detected with this method. To determine the jump delays for various jump distances, the galvo scanner was moved in a pattern, simulating the printing process. The control signal consisted of many small steps equal to a typical line spacing distance, each lasting for half the period of the resonant scanner and one larger step in between the jump. The measurement from the PSD was then compared to the control signal, and the jump delay was determined as the time needed for the lag time between the control signal and the measured position to return to the level observed before the jump. The accuracy of the measured jump delays was verified by printing  $100 \times 100 \times 100 \mu\text{m}^3$  cubes at increasing distances in between with fixed jump delays until an incorrectly positioned line appeared between the cubes.

## 2.7. Verification of the quality of produced 3D structures

The tests to confirm the quality of the 3D structures across the FOV were performed by producing microscallops with DEGRAD INX. The 300  $\mu\text{m}$  diameter structures were arranged in a  $7 \times 7$  array with a spacing of 50  $\mu\text{m}$  and printed with line spacing  $dX = 1.3 \mu\text{m}$ , layer spacing  $dZ = 1.9 \mu\text{m}$  and laser power  $P = 450 \text{ mW}$ . The microscallops were connected to the coverslip by printing a  $300 \times 300 \times 50 \mu\text{m}^3$  block structure with a laser power of 200 mW underneath them onto the glass surface. Different powers for microscallops and block structures were selected, due to the different processing windows. Stable bulk structures, such as cubes, can be created in the range between 120 mW and 350 mW, while higher power leads to thermal damage noticeable by bubble formation. Microscallops are stable at a minimum of 390 mW and show no thermal damage within the available power limits of the presented system. After developing the sample, it was sputtered with a layer of gold and imaged with a scanning electron microscope (EVO, Zeiss). The microscallops' strut widths were estimated from images taken at  $0^\circ$  to the z-axis, while the height was calculated from values measured at  $45^\circ$ .

## 2.8. Throughput optimization

All tests were performed with the previously determined optimal line and layer spacing of 1.3  $\mu\text{m}$  and 1.9  $\mu\text{m}$  and were run without resin. For each array size 3 layers of microscallops were produced and the number of tiles in XY was selected such that the total number of microscallops was always around 2100. Each set of parameters was run with sample rates of 30 MSamples/s and 60 MSamples/s to show the limiting influence of the AWG's data transfer rate on the throughput.

## 3. Results

### 3.1. Hardware & optics

The newly developed 2PP setup is based on a 8 kHz resonant mirror scanner which deflects the laser during the fabrication process. This configuration offers the potential for rapid production of microscallops and to achieve scan speeds almost two orders of magnitude higher than those of previously reported with 2PP systems based on galvo scanners [12]. However, due to the nature of the resonant scanner, which oscillates at a defined frequency, position and speed control are limited. To accommodate for this constraint and still fully exploit the potential of high speed 2PP fabrication, careful selection and optimization of the setup's components are crucial (Fig. 1). Additionally, when using high scanning speeds, the system has to deliver a sufficient light dose to achieve 2PP despite the short exposure duration of each voxel and the acousto optic modulator (AOM) must exhibit rapid light intensity modulation to maintain 2PP accuracy along the scan direction. Further, the optics must provide a large FOV, in order to minimize the contribution of the stage movement on the overall structuring time.

In 2PP, structures are produced by sequential exposure of single voxels. This method creates an inherent conflict between throughput, feature size and positioning precision. The smallest achievable feature size is mainly determined by the optical components of a 2PP system. Specifically, by the numerical aperture of the objective, which determines how tightly the laser beam can be focused. However, when using a fast-scanning mirror, the feature size might increase along the scan direction despite the characteristics of the focusing optics, if the laser cannot be switched on and off fast enough leading to extended illumination duration.

Most modern 2PP setups, including the one presented in this work, use an AOM for laser beam attenuation as well as fast switching [37], which is determined by the AOM's modulation bandwidth. In systems with 2 galvo scanners, this doesn't usually affect the resolution along the scan path since the maximum achievable scanning speed is not in

conflict with the modulation bandwidth of the AOM. For instance, in the case of a set-up based on two galvo scanners which are scanning with a speed of 0.6 m/s the focal spot only moves 300 nm in the time it takes an AOM with a modulation bandwidth of 1 MHz to switch on and off again. In this case the feature size is mainly determined by the focusing optics. However, when using a maximum scan speed of 66.6 m/s as in the 2PP setup presented in this work, a modulation bandwidth of more than 100 MHz would be necessary to achieve the same result. AOMs with such high modulation bandwidth do not exist, and the AOM becomes the limiting factor for the minimum feature size along the scan direction.

The modulation bandwidth mainly results from how fast the acoustic wave inside the AOM's crystal travels through the width of the laser beam so that the beam experiences the same level of diffraction across its whole cross-section when the wave's amplitude is modified. Therefore, the two ways to increase the modulation bandwidth are to either increase the speed of the acoustic wave or decrease the beam width. The former option is not viable, as the speed of sound doesn't vary enough between different materials suitable for AOMs, and the choice of material is usually made based on other factors such as optical wavelength, desired dispersion, and the required optical damage threshold [38]. On the other hand, reducing the beam width is more straightforward to achieve but comes with new challenges. A smaller, more divergent beam reduces the AOM's efficiency [39], and focusing the laser beam increases the intensity and could damage the crystal. As a compromise, in the presented set-up the laser beam is focused to roughly 250  $\mu\text{m}$  achieving an efficiency of 55 %.

To test the modulation bandwidth the AOM was turned on twice for a defined time, including a break of the same duration between the created pulses. The resulting laser modulation was recorded with a photodiode. The selected time intervals were multiples of the output duration of a single sample at the maximum sample rate of the arbitrary waveform generator (AWG) that controls the AOM. Fig. 2a shows that using a pulse duration of a single sample (16 ns), the modulated laser does not reach the desired amplitude, and consecutive pulses are merged into one. When the pulses last 2 samples (32 ns) (Fig. 2b), the pulse reaches almost full amplitude, and the following pulse is clearly separated. Therefore, the modulation bandwidth is roughly 15 MHz.

A common practice to determine the minimum achievable feature size of a setup is to assess the printing of single-voxel lines [36,40,41]. Writing lines parallel to the resonant scanner's scan direction using a 10x objective led to a line width of 0.97  $\mu\text{m}$  or less (Fig. 2c). When structuring perpendicular to the scanning direction (Fig. 2d) the AOM as a limiting factor becomes apparent. Despite using the optimized bandwidth, the line width increased at the center of the FOV, where the scan velocity is the highest, to values between 1.38  $\mu\text{m}$  and 2.17  $\mu\text{m}$ . Although resolution is sacrificed in favor of fabrication speed this tradeoff is acceptable, as the attainable feature size proves to be more than sufficient for the intended application of producing microscallops. Nevertheless, if higher resolution is desired, it can be achieved by either employing a higher magnification objective or reducing the scan range and, consequently, the scan speed. In both scenarios, there would be a reduction in throughput.

The lower uniformity of the perpendicular lines is attributed to the need to create them from individual voxels in separate scan lines, which introduces precision issues. The accuracy of a 2PP system is determined, on the one hand, by the achievable feature size, on the other hand, by the positioning precision. Although feature size becomes less critical for structures lacking fine features, positioning precision remains crucial for all structure dimensions, as low precision may result in aliasing and rough surfaces. The positioning precision along the scan direction is determined by the AGW's sample rate. In the setup presented in this work, with a maximum rate of 62.5 MSamples/s, the AWG's trigger events are uniformly distributed within 16 ns after the rise of the trigger signal. This leads to a positioning precision of 1.07  $\mu\text{m}$  at the FOV's center, where the scan speed is highest. This also accounts for the lower uniformity observed in the line tests of perpendicular lines compared to

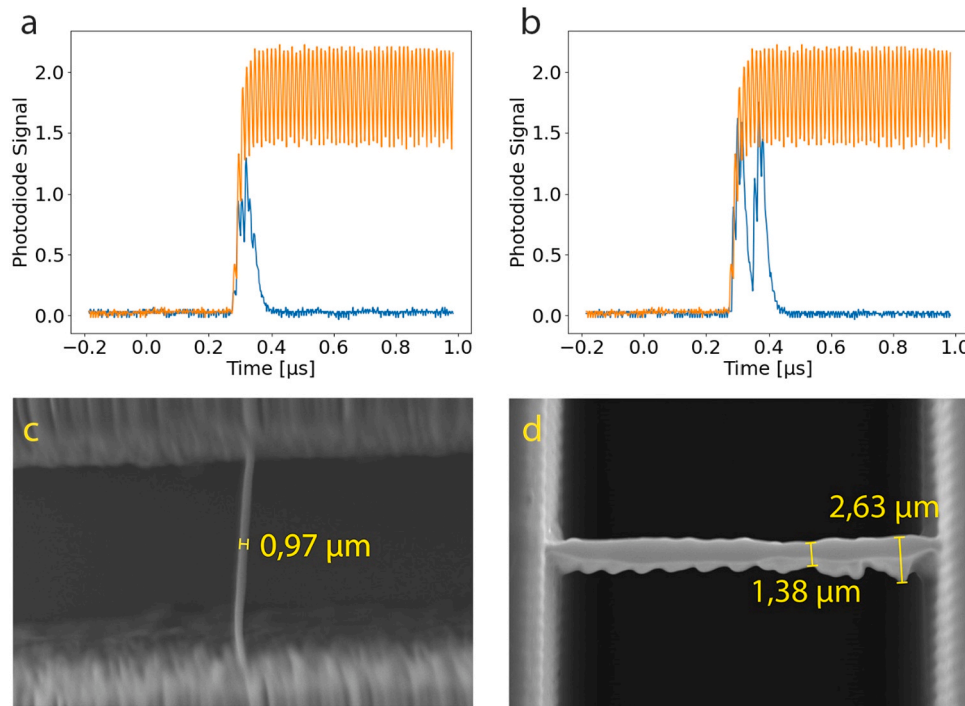


**Fig. 2. AOM bandwidth measurement and Line tests:** (a) blue: measured laser amplitude when driving the AOM with two 16 ns pulses (blue) compared with a single switch-on process (orange). The pulses cannot be discerned, and the signal never reaches full amplitude. The oscillation within the signals is caused by the laser's 80 MHz repetition rate. (b) Bandwidth test with 32 ns pulses. The pulses are clearly distinguishable and reach full amplitude, indicating a modulation bandwidth of 30 MHz. SEM images of a 20  $\mu\text{m}$  long single-voxel line printed (c) along the scan direction with a width of 0,97  $\mu\text{m}$ . (d) perpendicular to the scan direction by single voxels in consecutive scan lines.

those parallel to the scan direction, as neighboring voxels may be slightly shifted relative to each other.

### 3.2. Calibration

#### 3.2.1. Resonant movement correction and synchronization

The resonant scanner's high scan velocity and non-linear motion require it to be precisely synchronized with the AOM. Discrepancies between the assumed and the actual focus position at the moment of material exposure will not only lead to a shifted, but also a distorted structure due to the sinusoidal movement of the scanner. Furthermore, when scanning bidirectionally, timing errors can cause misalignment between lines produced in opposite directions, leading to fragmented or frayed lines at the edges of the structure.

Synchronization between the resonant scanner and AOM is achieved with a TTL signal from the scanner's driver that switches level at the scanner's turnaround point. This turnaround point is used as a reference point to calculate the output signal along a line. To ensure accurate synchronization, several key characteristics of the setup need to be determined: the precise frequency of the resonant scanner, a sync delay that corrects for the offset between the sync signal and the point in time where the output should be triggered, and the scanner's FOV size.

The frequency can be measured by recording the power distribution across the FOV. This is achieved by capturing the power using a photodiode over the duration of a single line and repeating the process for a range of galvo scanner positions. The resulting signal is mirrored at the resonant scanner's turnaround points. Therefore, the time difference between those mirror points is equal to half the resonant scanner's period. The scan frequency given in the specifications as  $7910 \pm 10$  Hz was determined to be 7906 Hz. Furthermore, the measurement can be used to detect an offset between the sync signal and the actual turnaround point, which must be compensated by the aforementioned sync delay. The offset fell within the range of 600 ns.

Another factor that leads to the need for a sync delay is the AOM's

response time, which can be measured from the data acquired during the bandwidth measurement described in 3.1. Throughout this measurement, the oscilloscope was triggered by the AOM control signal, and the response time was determined as the period between the trigger point and the moment at which the laser power reached the specified amplitude. As shown in Fig. 2a&b, the measurement showed this to be approximately 300 ns. The reaction time between sending the control signal to the AOM and the diffracted laser beam reaching the set amplitude largely arises from the time taken for the acoustic wave in the crystal to propagate from the piezoelectric transducer to and through the laser beam. It depends on the beam diameter and the position at which the laser crosses the crystal and requires re-evaluation after each alignment of the AOM.

Instead of analyzing all the factors that add up to the sync delay individually after each alignment, it has proven to be faster to determine the sync delay by producing test structures. By scanning single layers of parallel lines with varying delays, the setting at which the lines from both print directions fully overlap can be identified. This assessment can be conveniently made by observing the structures through the setup's camera (Fig. 3a). Upon repeating this process for various sample rates (Fig. 3b), it was observed that the delay in samples scales linearly with the sample rate. This would be expected if the delay in seconds was independent of the sample rate, however, the delay exhibits an additional constant offset of 16 samples, likely caused by a trigger delay of the AWG. The sample rate independent share of the sync delay amounts to 900 ns, a value that aligns well with the sum of AOM response time and the offset between the sync signal and the actual turnaround point.

#### 3.2.2. Scaling

Upon establishing synchronization between components, determining the correct position of the laser focus within the image plane from the angular position of the scan mirrors is crucial for creating accurately scaled structures. To achieve this, separate scaling factors for each scan direction are used. The maximum scan distances in the

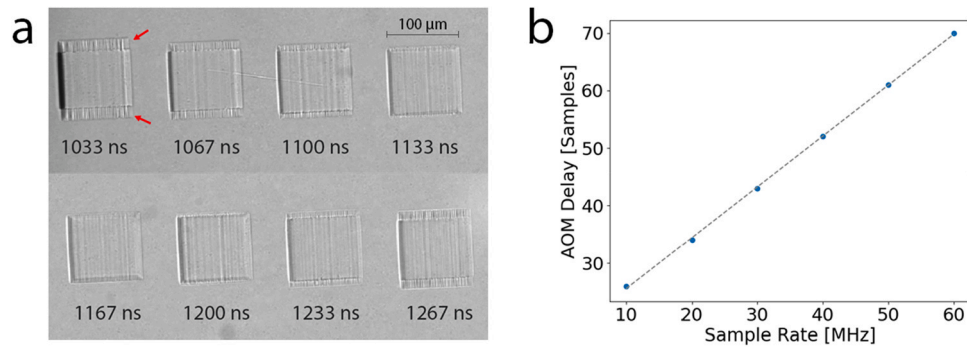


**Fig. 3. Sync delay:** (a) comparison of different synchronization delay settings (1033–1267 ns / 62 – 76 samples) at a sample rate of 60 MSamples/s; incorrect delay settings lead to frayed lines at the object's edges (indicated by red arrows for one of the squares), while using the correct delay (1167 ns) a clean square is created; (b) linear increase of delay duration with increasing sample rate. The fixed offset indicates a trigger delay of the AWG.

printing plane for each direction were chosen as variable factors, to provide a more intuitive understanding of the values than simple fractional values. As a starting point, a value of 2723  $\mu\text{m}$  was calculated based on available hardware and optics specifications. More precise values were then determined by producing a single-layer square structure, moving the XY-stage by the intended size of the square, using the stage as a reference, and then producing a second square. If the squares' edges were not aligned precisely, the scaling parameter had to be adjusted and the process was repeated. The maximum scan distances obtained through this method were 2710  $\mu\text{m}$  for the slow-scanning X-direction and 2690  $\mu\text{m}$  for the fast-scanning Y-direction. The deviation from the theoretical value can be attributed to the assumption that the scanner, scan and tube lens, and objective would be arranged in an ideal 4f-configuration, while the actual optical setup slightly deviates from such an arrangement.

### 3.2.3. Galvo movement characterization

In a system with 2 non-resonant galvo mirrors, synchronization and positioning of the slower-axis mirror is of minimal concern due to the jump delay determined for the faster-axis mirror being sufficient. However, when combined with a 8 kHz resonant scanner, the galvo mirror responsible for switching between line positions, has to operate close to its limits. When subsequent lines are required to be separated by more than the line spacing, a jump delay becomes necessary to ensure the correct positioning of printed lines after the jump. Failure to implement this would result in incorrectly printed lines visible as a ghosting effect (Fig. 4a) due to the galvo scanner's inability to cover the distance quickly enough. All delays are discussed as a number of lines, as the output can only be shifted by the full scan duration of a line, with each line equivalent to 63  $\mu\text{s}$  due to the fixed scan frequency. To cover all possible jump distances up to the full width of a FOV (1305  $\mu\text{m}$ ), a delay of 8 lines (505  $\mu\text{s}$ ) would be necessary. However, this would significantly impact the processing time, especially for structures with multiple jumps

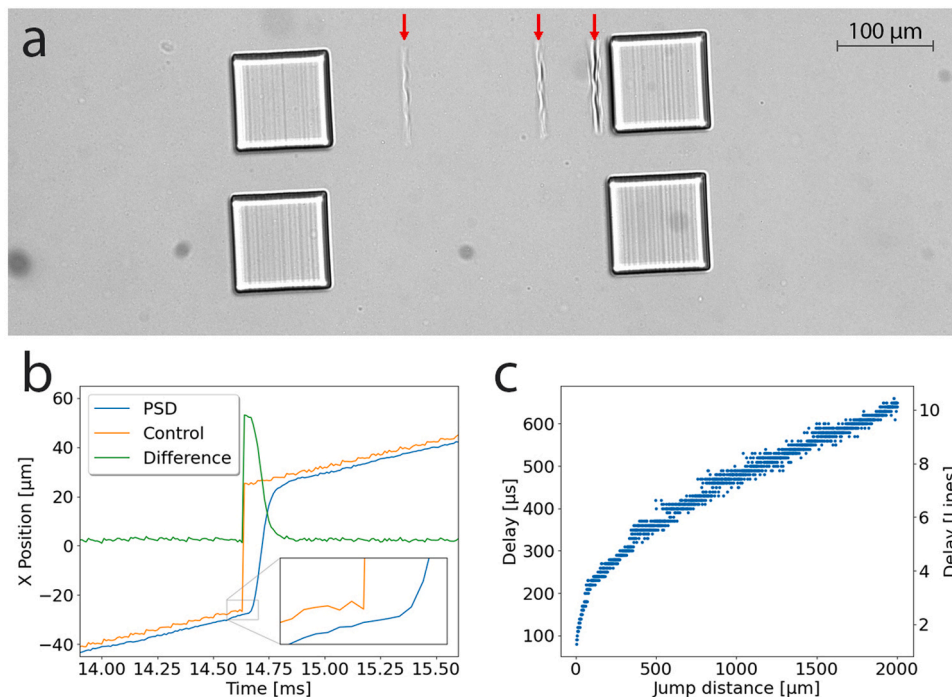


**Fig. 4. Galvo scanner jump delay evaluation:** (a) Cubes produced for the manual evaluation of jump delays, with incorrect (top) and correct settings (bottom); The incorrectly placed lines resulting from the incorrect delay are marked by red arrows. (b) Comparison between the galvo scanner control signal (orange) and the actual position of the scanner measured with a PSD sensor (blue). The scanner doesn't follow the step shape and moves with a delay. The plot shows the behavior of the galvo scanner during a 50  $\mu\text{m}$  jump. The necessary jump delay is determined as the time needed for the difference (green) between galvo position and control signal to return to the level before the jump. The zoomed in section shows the response delay. (c) The measured jump delays for each jump distance.

per layer. As a result, the minimum delay was determined for different jump distances using a measurement method involving a PSD sensor.

The measurement showed that even when scanning evenly spaced lines with a typical line spacing of 0.5–1.5  $\mu\text{m}$ , the galvo scanner is not able to follow the step shape of the control signal, but instead moves at constant speed (Fig. 4b) mainly due to its limited bandwidth. Jump delays were measured for jump distances from 5  $\mu\text{m}$  to 2000  $\mu\text{m}$  in 1  $\mu\text{m}$  steps. For jump distances of less than 500  $\mu\text{m}$  the jump delays roughly increase with the square root of the distance, while the relation becomes more linear for larger distances. This suggests that the scanner is accelerating throughout the whole duration of the smaller jumps, while the maximum scanner velocity is reached during larger jumps. Furthermore, the lowest measured jump delay is two lines. A closer look at the measurement curve reveals that this is due to the response time of the galvo scanner, which is approximately 60  $\mu\text{s}$  (Fig. 4b).

By shifting the galvo's control signal by the scan duration of one line relative to the AOM's signal, all jump delays can be reduced by an additional line.

In order to validate the PSD-based measurement, cubes were produced at various distances to determine the jump delay manually (Fig. 4a). The values obtained through this manual method closely matched the previous automated measurement. However, solely relying on the end result would not allow for a distinction between the galvo's response time and the actual jump delay. Consequently, the PSD measurement indicated one line shorter jump delays, resulting in a 4.4 % reduction in scan time for the production of 300  $\mu\text{m}$  microscaffolds. Therefore, the PSD measurement method offers a notable advantage over the more traditional approach of using test prints to determine processing parameters.

### 3.2.4. FOV power distribution

While the high scan speed reduces the cumulative scan time, other factors such as the stage movement between layers and FOVs begin to contribute significantly to the total print duration. The stage movement scales linearly with the number of FOVs and becomes a substantial portion of the total processing time. To effectively minimize the time

spent waiting for stage movements to complete, the number of FOVs needs to be reduced by increasing their area.

However, this approach necessitates an assessment of the potential variations in polymerization threshold across the FOV. The polymerization efficiency is affected by the voxel shape given by the objective's point spread function and the amount of power that is focused within the voxel. Typically, both deteriorate towards the edge of the FOV due to distortions and suboptimal laser alignment. Using optimized optics, aberrations can be minimized, thereby enhancing polymerization efficiency. Additionally, the quality of laser alignment was verified through the FOV power measurement described in Section (3.2.1), which includes assessing the uniformity of the power distribution across the FOV and identifying whether the maximum intensity aligns with the FOV center. The power distribution in a well-aligned setup (Fig. 5a) should consist of a central, predominantly uniform section, where the laser beam passes unhindered through all optical components, followed by a circular power drop-off beyond a certain radius, reflecting partial blockage of the laser beam at large scan angles.

This method, allows for the detection of misalignments and errors in the mounting of optical components. Fig. 5a shows the power distribution in the FOV of a well-aligned set-up. The maximum intensity was offset along the Y-axis, due to the resonant scan mirror being overfilled by the laser beam, resulting in a varying aperture based on the mirror's angle. Practical tests showed that for power values far above the polymerization threshold, structures of uniform quality can be produced across the FOV.

Produced microscaffolds were examined using a SEM to evaluate whether the FOV optimization translates well to practical applications. Producing  $7 \times 7$  microscaffolds covering an area of  $2400 \times 2400 \mu\text{m}^2$  within a single FOV, resulted in nearly complete filling of the objective FOV, with the microscaffolds at the corners being produced outside the actual objective FOV. However, all microscaffolds were self-supporting, and only those outside the objective's FOV showed noticeable signs of reduced quality due to optical distortions (Fig. 5b). Comparing the strut sizes to the CAD design showed that the width of  $12.8 \pm 0.4 \mu\text{m}$  closely matches the design's 14.6  $\mu\text{m}$  (Fig. 5c). Nonetheless, a higher deviation

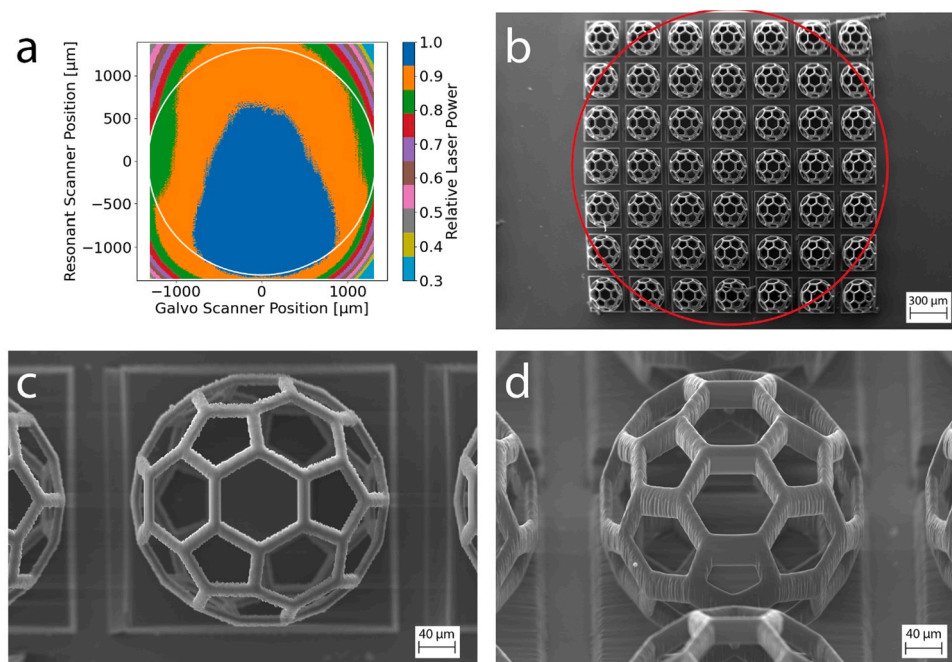


**Fig. 5. SEM images of produced microsccaffold:** (a) The setup's power distribution across the FOV; The power stays above 80 % of the maximum across the objective's whole FOV of 2650  $\mu\text{m}$  (white circle). (b) Overview of  $7 \times 7$  microscaffolds printed within one FOV. The red circle indicates the objective FOV of 2650  $\mu\text{m}$ . (c) Top view of the microsccaffold in the center of the FOV. (d) 45-degree view of the central microsccaffold. The struts are slightly elongated along the Z-direction, as expected when using the implemented focusing optics.

was observed in the Z-direction, where the strut height of  $28.4 \pm 2.9 \mu\text{m}$  was more than twice the design's  $12.9 \mu\text{m}$  (Fig. 5d). This effect is expected with low numerical aperture objectives due to the in Z-direction elongated voxel shape.

### 3.3. Throughput optimization

When analyzing various 3D printers, summarizing the throughput in a single easily comparable number is not feasible. Instead, a comprehensive understanding of the factors contributing to the cumulative processing speed increase and their potential drawbacks is necessary. For instance, in the case of 2PP, the tradeoff between throughput and resolution, is a fundamental consideration. The volumetric throughput of a 2PP system can be changed by multiple orders of magnitude by simply using different objectives to focus the laser beam, and the potential tradeoff should always be based on the considerations of a specific application. In the following, various aspects of the 2PP process will be examined, each of which can significantly impact the total throughput. To evaluate the throughput the fabrication of micro-scaffolds will be used as a benchmark test. This choice is justified by the complex geometry and fine struts of the micro-scaffolds, making them a challenging structure to produce with 2PP, let alone any other technology. It can be assumed that performance for less complex designs would be at least equivalent or even better. After developing the samples, it is possible to assess the quality of the produced structures for signs of insufficient polymerization. Factors such as incorrectly selected processing parameters, distortion of the laser beam, or inadequate illumination of the FOV can result in insufficient photon densities resulting in a weak polymer network leading to mechanically unstable structures that are prone to deformation or collapsing. Moreover, the production of micro-scaffolds and according parameters are well established on other 2PP systems[42], enabling a comparison between the presented setup and a system with two galvo scanners that performs similarly to the current generation of commercial systems.

#### 3.3.1. Microscaffold arrangement

Optimizing the arrangement of structures within the FOV is essential for ensuring their high quality and maximizing the throughput.

Considering the unique micro-scaffold design, careful thought was given to the orientation of the CAD model of single micro-scaffolds to minimize the number of required line scans. This can be accomplished by aligning the micro-scaffold so that the scanning direction is perpendicular to one of its 15 planes of reflection symmetry. This is because the orthographic projection of a micro-scaffold onto one of its mirror planes yields a smaller area compared to projections in other orientations. Consequently, there remains a single rotational degree of freedom along the scan direction, allowing to choose between different micro-scaffold orientations. Subsequent 2PP tests, however, revealed that this orientation had no impact on the process duration. Consequently, an orientation was selected where one of the structure's hexagons was aligned parallel to the focal plane. This orientation facilitates easier attachment of micro-scaffolds to the glass substrate during characterization tests (Fig. 5). This improved orientation with an optimally positioned mirror plane requires 33 % less scan time than the same micro-scaffold rotated by 90 ° around the Z-axis.

In 2PP systems with 2 galvo scanners, the print area is typically chosen to be a square, maximizing the usable area within the circular objective FOV and reducing stage movements for separate FOVs. However, considering the fixed line rate of a resonant scanner, it is more advantageous to use a rectangular FOV elongated along the fast-scanning axis. As outlined in 3.2.4, although it is possible to produce structures that exceed the objective FOV, however, it is advisable to regard the objective FOV as the upper limit for the processing area in order to avoid optical aberrations and ensure structure quality.

In context of optimizing throughput, the consideration of the scan rate alone would suggest the use of very narrow FOVs in X-direction to

maximize the usable length in Y-direction. However, it is essential to also account for the movement time of the Z-stage between each layer. Splitting the processing area into smaller FOVs that are optimized for scan time, would result in an increase in total Z-stage movement time. Therefore, those two factors have to be balanced. Calculations showed that for producing bulk structures with an average Z-stage movement duration of 25 ms between layers, the optimal FOV size would be  $1440 \times 2220 \mu\text{m}^2$ . When arranging  $300 \mu\text{m}$  micro-scaffolds spaced  $35 \mu\text{m}$  apart, the arrangement of an array of  $4 \times 7$  structures (maximum distance from center:  $1300 \mu\text{m}$ ) closely approximates this optimal value. To confirm that this would be the optimum array size, tests were conducted to measure the average throughput for different array sizes. The results are presented in Table 1.

Using the previously reported standard arrangement of  $3 \times 3$  of micro-scaffolds[42] facilitated a throughput rate of 4644 structures per hour. Therefore, transitioning to a resonant scanner, while maintaining all other processing parameters, yielded a 22.4-fold increase over the previous throughput of 208 micro-scaffolds/h. Furthermore, it was observed that arrays of  $5 \times 5$  micro-scaffolds, representing the largest square arrangement feasible within the FOV, more than doubled the throughput. Additionally, optimizing for a single scan direction of  $4 \times 7$  structures resulted in a 23 % increase in throughput, achieving an hourly throughput of 12,078 micro-scaffolds, which is 57 times faster than the setup based on two galvo mirrors. A video of the optimized production process can be found in the [supplementary material](#). Notably, elongation of the scan area in the scan direction was found to significantly enhance throughput. Conversely, the 90-degree rotated array of  $7 \times 4$  micro-scaffolds exhibited a performance inferior to that of the square array, as anticipated.

Supplementary material related to this article can be found online at [doi:10.1016/j.addma.2024.104601](https://doi.org/10.1016/j.addma.2024.104601).

#### 3.3.2. Data transfer speed

During 2PP of a single FOV, the control signal data is transferred from the PC's memory to the AWG's internal memory while the Z-stage moves to the next layer's position. Once both of these processes have finished, the layer is produced. This means that while the Z-stage typically limits the throughput, the data transfer becomes a bottleneck when the amount of data per layer becomes too large. This effect becomes evident when comparing the processing time for different sample rates as shown in Table 1. For instance, when using a rate of 30 MSamples/s instead of 60 MSamples/s, the amount of data is halved and is no longer limiting the throughput.

Furthermore, the bottleneck effect is more pronounced for larger numbers of micro-scaffolds in the X-direction, given the greater number of lines and, hence, a larger amount of data. However, reducing the sample rate also impacts the positioning resolution, and a potential loss in structure quality has to be weighed against the need for high throughput. A potential solution to this tradeoff could be the use of a newer AWG model in a revised setup, as the available data transfer speed has increased by more than a factor 4.

## 4. Discussion and outlook

The unrivaled resolution and precision of 2PP, compared to other additive manufacturing methods, makes it an interesting option for numerous applications. However, its relatively low throughput still presents a challenge for large-scale production. The setup presented in this study demonstrates the steps that can be taken to address this limitation. Utilizing an 8 kHz resonant scanner enables unprecedented scanning speeds of up to 66 m/s. Coupling with a high-power 515 nm laser allows the use of efficient UV photoinitiators, enabling effective 2PP even at the highest scan speeds. The optical system was designed to ensure uniform power distribution across a large scan area. Careful consideration of the modulation bandwidth was taken into account in the selection of the setup's AOM to facilitate the production of small

**Table 1**  
Processing time comparison between differently sized arrays of microscaffolds.

Array size	Total number of microscaffolds	30 MSamples/s		60 MSamples/s	
		Processing time [s]	Microscaffolds/s	Processing time [s]	Microscaffolds /s
3 × 3	2160	1670	1293	1836	1176
5 × 5	2100	772	2720	981	2141
4 × 7	2100	626	3355	736	2853
7 × 4	2100	875	2400	1176	1786

feature sizes along the scan direction. Following the construction of the setup, a variety of newly developed measurement techniques were implemented to validate the calculated specifications and provide the calibration data necessary to optimize the setup to peak performance.

The AOM modulation bandwidth has been determined to be 30 MHz, resulting in a minimum feature size of 2.17  $\mu\text{m}$  at the position with the highest achievable scan velocity. Analysis of the power distribution across the FOV allowed to optimize for a predominantly uniform power distribution. Additionally, the precise frequency of the resonant scanner, essential for correct output calculation, can be determined from the same measurement. The synchronization delay necessary for correct positioning and bidirectional printing was identified via straightforward and quick-to-perform print tests. Analyzing the galvo scanner's movement allowed for minimizing the delays during jumps. Further optimization of the 2PP production speed included optimizing the orientation of CAD-models, their arrangement within the scan area, and the amount of data transferred to the setup's AWG.

The combination of these advancements led to a remarkable increase in throughput, achieving a 5700 % improvement over previously reported examples. In the specific use-case of microscaffolds for tissue engineering, this is expected to substantially reduce production times for larger in-vivo studies from weeks to hours.

In this work, the production of microscaffolds for tissue engineering was optimized, part of this optimization was selection of an appropriate focussing optics, allowing to obtain a relatively large FOV while maintaining feature sizes down to 0.97  $\mu\text{m}$ . This achieved resolution was adequate for the specific application and remains unmatched by other 3D printing technologies, such as  $\mu\text{SLA}$ [23]. Nevertheless, numerous other applications could benefit from increased throughput alongside the higher resolution characteristic of 2PP. To create structures with finer feature sizes, it would be feasible to increase the resolution by using objectives with higher numerical aperture and optimizing the setup accordingly. Table 2 summarizes the expected performance of the system using a 40x N.A. 0.95 and a 63x N.A. 1.4 objective, based on calculated values. The performance is compared to values reported from commercially available 2PP systems. Since the resonant scanning had no impact on the line and layer-spacing, a significant improvement in throughput can be expected when using higher numerical aperture objectives.

One application area that would greatly benefit from increased throughput is the fabrication of upscaled 2PP structures that extend beyond a single FOV in size. This approach necessitates precise stitching between FOVs. In the presented use case the size of the single microscaffolds did not require stitching, and consequently, the system was not optimized for this application. However, to implement stitching effectively, several factors must be considered to ensure the production of high-quality structures.

To achieve precise stitching, it is crucial to carefully determine the scaling factors and to ensure that the objective's image plane is accurately aligned with the stage movement plane to prevent any tilt between the blocks printed in individual FOVs. To maintain the high throughput demonstrated in this work, it is necessary to use the maximum FOV size. As distortion becomes more pronounced for large FOVs, additional distortion correction would be required to reduce stitching imperfections. While such a correction may slightly impact the fabrication speed due to potentially requiring additional scan lines, this

**Table 2**  
Performance comparison between 10x, 40x and 63x objectives.

	10x NA 0.4	40x NA 0.95	63x NA 1.4
Scan speed with galvo scanner	0.6 m/s [19]	0.15 m/s [19]	0.01 m/s [43]
Max. scan speed with resonant scanner	66.6 m/s	16.6 m/s	9.8 m/s
Typical line spacing	1.30 $\mu\text{m}$	0.17 $\mu\text{m}$ [19]	0.20 $\mu\text{m}$ [43]
Position precision along scan direction	1.07 $\mu\text{m}$	0.27 $\mu\text{m}$	0.33 $\mu\text{m}$

effect would still be significantly outweighed by the enhanced speed of a resonant scanner compared to a galvo scanner.

The current setup demonstrates a significant increase in throughput compared to previous generations of printers demonstrating the potential of resonant scanning in 2PP for a wide range of applications. However, there are still some challenges that need to be considered in the future.

One notable challenge is the variation in exposure time across the FOV due to the sinusoidal movement of the resonant scanner. While this may often be a minor concern, it can present difficulties for applications requiring precise control over exposure time and intensity, such as grayscale lithography [6,44]. To mitigate this issue, additional calibration methods will need to be implemented. Moreover, as discussed in chapter 3.3.1 throughput is reduced if the scan lines are not fully used. With two galvo scanners, the scan direction can be selected arbitrarily to optimize the structure arrangement. In contrast, full throughput with a resonant scanner can only be achieved by changing the structure arrangement accordingly, which presents an additional challenge to the control software in enabling adaptive CAD arrangements.

While increasing the scan speed has been a successful approach, future enhancements in this regard may prove challenging due to the limiting factor of the modulation bandwidth of the AOM. Strategies such as employing multiple beams in combination with high-speed scanning may prove advantageous for fabricating periodic structures, such as arrays of microscaffolds.

#### CRediT authorship contribution statement

**Aleksandr Ovsianikov:** Writing – review & editing, Supervision, Project administration, Funding acquisition, Conceptualization. **Tommaso Zandrini:** Supervision. **Han Woong Yoo:** Resources, Methodology. **Franziska Chalupa-Gantner:** Writing – review & editing, Supervision. **Stefan Binder:** Writing – original draft, Visualization, Software, Methodology, Investigation, Data curation, Conceptualization.

#### Declaration of Competing Interest

The authors declare that they have no known competing financial interests or personal relationships that could have appeared to influence the work reported in this paper

## Acknowledgments

This work was supported by the European Research Council (ERC) under the European Union's Horizon 2020 Research and Innovation Programme [Grant agreement No. 772464]. The authors acknowledge TU Wien Bibliothek for financial support through its Open Access Funding Programme.

## Appendix A. Supporting information

Supplementary data associated with this article can be found in the online version at [doi:10.1016/j.addma.2024.104601](https://doi.org/10.1016/j.addma.2024.104601).

## Data availability

Data will be made available on request.

## References

- [1] J. Stampfl, R. Liska, A. Ovsianikov, *Multiphoton lithography: techniques, materials, and applications*, John Wiley & Sons, 2016.
- [2] H. Wang, W. Zhang, D. Ladika, H. Yu, D. Gailevičius, H. Wang, C.F. Pan, P.N. S. Nair, Y. Ke, T. Mori, J.Y.E. Chan, Q. Ruan, M. Parsari, M. Malinauskas, S. Juodkazis, M. Gu, J.K.W. Yang, *Two-Photon polymerization lithography for optics and photonics: fundamentals, materials, technologies, and applications*, *Adv. Funct. Mater.* 33 (2023), <https://doi.org/10.1002/adfm.202214211>.
- [3] G. Zyla, M. Farsari, *Frontiers of laser-based 3D printing: a perspective on multi-photon lithography*, *Laser Photon Rev.* (2024), <https://doi.org/10.1002/lpor.202301312>.
- [4] D. Gonzalez-Hernandez, S. Varapnickas, A. Bertoncini, C. Liberale, M. Malinauskas, *Micro-optics 3D printed via multi-photon laser lithography*, *Adv. Opt. Mater.* 11 (2023), <https://doi.org/10.1002/adom.202201701>.
- [5] S. Steenhusen, F. Burmeister, M. Groß, G. Domann, R. Houbertz, S. Nolte, *Heterogeneous microoptical structures with sub-micrometer precision*, *Thin Solid Films* 668 (2018) 74–80, <https://doi.org/10.1016/j.tsf.2018.09.013>.
- [6] T. Aderneuer, O. Fernández, R. Ferrini, *Two-photon grayscale lithography for free-form micro-optical arrays*, *Opt. Express* 29 (2021) 39511, <https://doi.org/10.1364/oe.440251>.
- [7] A.J.G. Otuka, N.B. Tomazio, K.T. Paula, C.R. Mendonça, *Two-photon polymerization: Functionalized microstructures, micro-resonators, and bio-scaffolds*, *Polym. (Basel)* 13 (2021), <https://doi.org/10.3390/polym13121994>.
- [8] D. Mandt, P. Gruber, M. Markovic, M. Tromayer, M. Rothbauer, S.R. Adam Kratz, S. F. Ali, J. Van Hoorick, W. Holthöner, S. Mühleder, P. Dubruel, S. Van Vlierberghe, P. Ertl, R. Liska, A. Ovsianikov, *Fabrication of biomimetic placental barrier structures within a microfluidic device utilizing two-photon polymerization*, *Int. J. Bioprint* 4 (2018), <https://doi.org/10.18063/IJB.v4i2.144>.
- [9] K.A. Heintz, M.E. Bregenzler, J.L. Mantle, K.H. Lee, J.L. West, J.H. Slater, *Fabrication of 3D biomimetic microfluidic networks in hydrogels*, *Adv. Health Mater.* 5 (2016) 2153–2160, <https://doi.org/10.1002/adhm.201600351>.
- [10] F. Perrucci, V. Bertana, S.L. Marasso, G. Scordo, S. Ferrero, C.F. Pirri, M. Cocuzza, A. El-Tamer, U. Hinze, B.N. Chichkov, G. Canavese, L. Scaltrito, *Optimization of a suspended two-photon polymerized microfluidic filtration system*, *Micro Eng.* 195 (2018) 95–100, <https://doi.org/10.1016/j.mee.2018.04.001>.
- [11] H.J. McLennan, A.J. Blanch, S.J. Wallace, L.J. Ritter, S.L. Heinrich, D.K. Gardner, K.R. Dunning, M.J. Gauvin, A.K. Love, J.G. Thompson, *Nano-liter perfusion microfluidic device made entirely by two-photon polymerization for dynamic cell culture with easy cell recovery*, *Sci. Rep.* 13 (2023), <https://doi.org/10.1038/s41598-023-27660-x>.
- [12] O. Guillaume, O. Kopinski-Grünwald, G. Weisgrab, T. Baumgartner, A. Arslan, K. Whitmore, S. Van Vlierberghe, A. Ovsianikov, *Hybrid spheroid micro-scaffolds as modular tissue units to build macro-tissue assemblies for tissue engineering*, *Acta Biomater.* 165 (2023) 72–85, <https://doi.org/10.1016/j.actbio.2022.03.010>.
- [13] M.A. Skylar-Scott, M.C. Liu, Y. Wu, A. Dixit, M.F. Yanik, *Guided homing of cells in multi-photon microfabricated bioscaffolds*, *Adv. Health Mater.* 5 (2016) 1233–1243, <https://doi.org/10.1002/adhm.201600082>.
- [14] A. Koroleva, S. Gittard, S. Schlie, A. Deiwick, S. Jockenhoefel, B. Chichkov, *Fabrication of fibrin scaffolds with controlled microscale architecture by a two-photon polymerization-micromolding technique*, *Biofabrication* 4 (2012), <https://doi.org/10.1088/1758-5082/4/1/015001>.
- [15] W. Wang, Z.Q. Chen, B. Lin, M.C. Liu, Y. Zhang, S.J. Liu, Y. Li, Q. Zhao, *Two-photon polymerization-based 3D micro-scaffolds toward biomedical devices*, *Chem. Eng. J.* 493 (2024), <https://doi.org/10.1016/j.cej.2024.152469>.
- [16] T. Zandrini, S. Florczak, R. Levato, A. Ovsianikov, *Breaking the resolution limits of 3D bioprinting: future opportunities and present challenges*, *Trends Biotechnol.* 41 (2023) 604–614, <https://doi.org/10.1016/j.tibtech.2022.10.009>.
- [17] M. Woletz, F. Chalupa-Gantner, B. Hager, A. Ricke, S. Mohammad, S. Binder, S. Baudis, A. Ovsianikov, C. Windischberger, Z. Nagy, *Toward printing the brain: a microstructural ground truth phantom for MRI*, *Adv. Mater. Technol.* 9 (2024), <https://doi.org/10.1002/admt.202300176>.
- [18] G. Weisgrab, O. Guillaume, Z. Guo, P. Heimel, P. Slezak, A. Poot, D. Grijpma, A. Ovsianikov, *3D printing of large-scale and highly porous biodegradable tissue engineering scaffolds from poly(trimethylene-carbonate) using two-photon-polymerization*, *Biofabrication* 12 (2020), <https://doi.org/10.1088/1758-5090/abb539>.
- [19] T. Koch, W. Zhang, T.T. Tran, Y. Wang, A. Mikitisin, J. Puchhammer, J.R. Greer, A. Ovsianikov, F. Chalupa-Gantner, M. Lunzer, *Approaching standardization: mechanical material testing of macroscopic two-photon polymerized specimens*, *Adv. Mater.* 36 (2024), <https://doi.org/10.1002/adma.202308497>.
- [20] S. Maruo, O. Nakamura, S. Kawata, *Three-dimensional microfabrication with two-photon-absorbed photopolymerization*, *Opt. Lett.* 22 (1997) 132–134.
- [21] A. Arslan, W. Steiger, P. Roose, H. Van den Bergen, P. Gruber, E. Zerbin, F. Gantner, O. Guillaume, A. Ovsianikov, S. Van Vlierberghe, P. Dubruel, *Polymer architecture as key to unprecedented high-resolution 3D-printing performance: The case of biodegradable hexa-functional telechelic urethane-based poly-ε-caprolactone*, *Mater. Today* 44 (2021) 25–39, <https://doi.org/10.1016/j.mattod.2020.10.005>.
- [22] J. Stampfl, S. Baudis, C. Heller, R. Liska, A. Neumeister, R. Kling, A. Ostendorf, M. Spitzbart, *Photopolymers with tunable mechanical properties processed by laser-based high-resolution stereolithography*, *J. Micromech. Microeng.* 18 (2008), <https://doi.org/10.1088/0960-1317/18/12/125014>.
- [23] J.M. Kronenfeld, L. Rother, M.A. Saccone, M.T. Dulay, J.M. DeSimone, *Roll-to-roll, high-resolution 3D printing of shape-specific particles*, *Nature* 627 (2024) 306–312, <https://doi.org/10.1038/s41586-024-07061-4>.
- [24] D. Loterie, P. Delrot, C. Moser, *High-resolution tomographic volumetric additive manufacturing*, *Nat. Commun.* 11 (2020), <https://doi.org/10.1038/s41467-020-14630-4>.
- [25] M. Regehly, Y. Garmshausen, M. Reuter, N.F. König, E. Israel, D.P. Kelly, C. Y. Chou, K. Koch, B. Asfari, S. Hecht, *Xolography for linear volumetric 3D printing*, *Nature* 588 (2020) 620–624, <https://doi.org/10.1038/s41586-020-3029-7>.
- [26] M. Shusteff, A.E.M. Browar, B.E. Kelly, J. Henriksson, T.H. Weisgraber, M. Panas, N.X. Fang, C.M. Spadaccini, *One-step volumetric additive manufacturing of complex polymer structures*, 2017. (<https://www.science.org>).
- [27] A. Ovsianikov, Z. Li, J. Torgersen, J. Stampfl, R. Liska, *Selective functionalization of 3D matrices via multiphoton grafting and subsequent click chemistry*, *Adv. Funct. Mater.* 22 (2012) 3429–3433, <https://doi.org/10.1002/adfm.201200419>.
- [28] F. Cantoni, D. Maher, E. Bosler, S. Kühne, L. Barbe, D. Oberschmidt, C. Marquette, R. Taboryski, M. Tenje, A.I. Bunea, *Round-robin testing of commercial two-photon polymerization 3D printers*, *Addit. Manuf.* 76 (2023), <https://doi.org/10.1016/j.addma.2023.103761>.
- [29] V. Hahn, P. Kiefer, T. Frenzel, J. Qu, E. Blasco, C. Barner-Kowollik, M. Wegener, *Rapid assembly of small materials building blocks (voxels) into large functional 3D metamaterials*, *Adv. Funct. Mater.* 30 (2020), <https://doi.org/10.1002/adfm.201907795>.
- [30] A. Balena, M. Bianco, F. Pisanello, M. De Vittorio, *Recent advances on high-speed and holographic two-photon direct laser writing*, *Adv. Funct. Mater.* 33 (2023), <https://doi.org/10.1002/adfm.202211773>.
- [31] E. Skliutas, M. Lebedevaite, E. Kabouraki, T. Baldacchini, J. Ostrauskaite, M. Vamvakaki, M. Farsari, S. Judozakis, M. Malinauskas, *Polymerization mechanisms initiated by spatio-temporally confined light*, *Nanophotonics* 10 (2021) 1211–1242, <https://doi.org/10.1515/nanoph-2020-0551>.
- [32] L. Zhang, C. Wang, C. Zhang, Y. Xue, Z. Ye, L. Xu, Y. Hu, J. Li, J. Chu, D. Wu, *High-throughput two-photon 3D printing enabled by holographic multi-foci high-speed scanning*, *Nano Lett.* 24 (2024) 2671–2679, <https://doi.org/10.1021/acs.nanolett.4c00505>.
- [33] W. Ouyang, X. Xu, W. Lu, N. Zhao, F. Han, S.C. Chen, *Ultrafast 3D nanofabrication via digital holography*, *Nat. Commun.* 14 (2023), <https://doi.org/10.1038/s41467-023-37163-y>.
- [34] B. Jiao, F. Chen, Y. Liu, X. Fan, S. Zeng, Q. Dong, L. Deng, H. Gao, W. Xiong, *Acousto-optic scanning spatial-switching multiphoton lithography*, *Int. J. Extrem. Manuf.* 5 (2023), <https://doi.org/10.1088/2631-7990/ace0a7>.
- [35] T. Zandrini, O. Shan, V. Parodi, G. Cerullo, M.T. Raimondi, R. Osellame, *Multi-foci laser microfabrication of 3D polymeric scaffolds for stem cell expansion in regenerative medicine*, *Sci. Rep.* 9 (2019), <https://doi.org/10.1038/s41598-019-48080-w>.
- [36] B.W. Pearce, C. Michas, J.M. Tsang, T.J. Gardner, T.M. Otchy, *Fast micron-scale 3D printing with a resonant-scanning two-photon microscope*, *Addit. Manuf.* 30 (2019), <https://doi.org/10.1016/j.addma.2019.100887>.
- [37] R. Houbertz, P. Declerck, S. Passinger, A. Ovsianikov, J. Serbin, B.N. Chichkov, *Investigations on the generation of photonic crystals using two-photon polymerization (2PP) of inorganic-organic hybrid polymers with ultra-short laser pulses*, *Phys. Status Solidi (a)* 204 (2007) 3662–3675.
- [38] A.N.Z. Rashed, *Best candidate materials for fast speed response and high transmission performance efficiency of acousto optic modulators*, *Opt. Quantum Electron* 46 (2014) 731–750, <https://doi.org/10.1007/s11082-012-9583-y>.
- [39] S.N. Antonov, A.L. Filatov, *Acousto-Optic Diffraction in Paratellurite by a Slow Acoustic Mode. Increase of Diffraction Efficiency of Divergent Light*, *Tech. Phys.* 63 (2018) 876–880, <https://doi.org/10.1134/S106378421806004X>.
- [40] T. Zandrini, N. Liaros, L.J. Jiang, Y.F. Lu, J.T. Fourkas, R. Osellame, T. Baldacchini, *Effect of the resin viscosity on the writing properties of two-photon polymerization*, *Opt. Mater. Express* 9 (2019) 2601, <https://doi.org/10.1364/ome.9.002601>.
- [41] A. Ovsianikov, J. Viertel, B. Chichkov, M. Oubaha, B. MacCraith, I. Sakellari, A. Giakoumaki, D. Gray, M. Vamvakaki, M. Farsari, others, *Ultra-low shrinkage hybrid photosensitive material for two-photon polymerization microfabrication*, *ACS Nano* 2 (2008) 2257–2262.

- [42] O. Kopinski-Grünwald, O. Guillaume, T. Ferner, B. Schädl, A. Ovsianikov, Scaffolded spheroids as building blocks for bottom-up cartilage tissue engineering show enhanced bioassembly dynamics, *Acta Biomater.* (2023), <https://doi.org/10.1016/j.actbio.2023.12.001>.
- [43] A.I. Bunea, N. del Castillo Iniesta, A. Droumpali, A.E. Wetzal, E. Engay, R. Taboryski, Micro 3D Printing by Two-Photon Polymerization: configurations and Parameters for the Nanoscribe System, *Micro* 1 (2021) 164–180, <https://doi.org/10.3390/micro1020013>.
- [44] L. Siegle, S. Ristok, H. Giessen, Complex aspherical singlet and doublet microoptics by grayscale 3D printing, *Opt. Express* 31 (2023) 4179, <https://doi.org/10.1364/oe.480472>.